

Exploring the zone of anisotropy and broken symmetries in DNA-mediated nanoparticle crystallization

Matthew N. O'Brien^{a,b,1}, Martin Girard^{c,1}, Hai-Xin Lin^{a,b}, Jaime A. Millan^{a,b,c}, Monica Olvera de la Cruz^{a,b,c}, Byeongdu Lee^d, and Chad A. Mirkin^{a,b,c,2}

^aDepartment of Chemistry, Northwestern University, Evanston, IL 60208; ^bInternational Institute for Nanotechnology, Northwestern University, Evanston, IL 60208; ^cDepartment of Materials Science and Engineering, Northwestern University, Evanston, IL 60208; and ^dX-Ray Science Division, Argonne National Laboratory, Argonne, IL 60439

Contributed by Chad A. Mirkin, July 22, 2016 (sent for review May 3, 2016; reviewed by A. Paul Alivisatos and Nicholas A. Kotov)

In this work, we present a joint experimental and molecular dynamics simulations effort to understand and map the crystallization behavior of polyhedral nanoparticles assembled via the interaction of DNA surface ligands. In these systems, we systematically investigated the interplay between the effects of particle core (via the particle symmetry and particle size) and ligands (via the ligand length) on crystallization behavior. This investigation revealed rich phase diagrams, previously unobserved phase transitions in polyhedral crystallization behavior, and an unexpected symmetry breaking in the ligand distribution on a particle surface. To understand these results, we introduce the concept of a zone of anisotropy, or the portion of the phase space where the anisotropy of the particle is preserved in the crystallization behavior. Through comparison of the zone of anisotropy for each particle we develop a foundational roadmap to guide future investigations.

nanomaterials | anisotropic nanoparticles | colloidal crystallization | DNA | broken symmetry

Over the past decade, major advances in the control of nanoparticle interactions have led to powerful methods to assemble colloidal crystals (1–9). A high degree of structural control can be achieved in these methods if surface-bound ligands are used as nanoscale bonding elements to control the specificity, spacing, and strength of interactions. DNA has emerged as a particularly versatile ligand whose chemically and structurally defined nature can be used to program the symmetry, lattice parameters, and habit of colloidal crystals (1, 2, 7, 10–19). The shape of the underlying nanoparticle influences the directionality of DNA interactions, which can result in correlated nanoparticle orientations and predictable crystal symmetries based on geometric considerations (7, 13, 16, 19, 20). However, predictive control can be lost if the DNA shell does not preserve the anisotropy of the particle core (13), and thus key questions pertain to (i) the phase space over which predictable directional interactions persist and (ii) the nature of the phase transitions that occur as the anisotropy of the particle disappears. Identifying this “zone of anisotropy” and the broken symmetries that form are critical to establish design rules for work with non-spherical particles and to develop nanostructured materials with controlled properties.

Herein, we systematically investigate the phase space encoded by particle symmetry, particle size (L), and DNA length (D) to understand and map where directional interactions persist (Fig. 1). We show that particle symmetry dictates the crystalline states that can be accessed and how easily changes in L and D affect phase transitions between these states, which include transitions in Bravais lattice (i.e., the symmetry of how the particles are arranged within the unit cell) and particle orientation. The concepts introduced herein provide a roadmap to understand and predict particle crystallization behavior toward the construction of functional nanoparticle-based materials.

To map the zone of anisotropy in DNA-mediated nanoparticle crystallization, three common polyhedra were investigated:

cubes, octahedra, and rhombic dodecahedra. These nanoparticles are primarily bound by a single crystallographic plane repeated across the structure 6, 8, or 12 times, respectively (Fig. 1A), and can be synthesized via a seed-mediated method that yields >95% of the desired shape with <5% variation in size (Fig. 1A) (21). Particle uniformity was rigorously analyzed with a recently reported and freely available program that algorithmically analyzes transmission electron microscopy (TEM) images to analytically determine nanoparticle structure (22). As-synthesized gold nanoparticles were densely functionalized with DNA, and subsequently DNA “linkers” of programmable length (tuned in rigid 12-nm, double-stranded segments) were hybridized to the surface-bound DNA. Each DNA linker possesses a short, single-stranded “sticky end” with a self-complementary sequence that extends into solution (Table S1). Together, this design yields polyvalent building blocks that connect to each other through the collective hybridization of many DNA sticky ends. To facilitate comparison between different shapes, surface area (SA) was used instead of L , because this number correlates with the number of DNA strands given a similar DNA density.

Crystals were formed by slowly annealing DNA-functionalized nanoparticles from high to low temperature, which results in a slow increase in supersaturation that ensures nanoparticles crystallize into their lowest free energy configuration (23). These crystals were analyzed in solution with small angle X-ray scattering (SAXS; Fig. S1 and Tables S2–S4) and in the solid state, after encapsulation in silica, with EM (Fig. S2). Scattering data were modeled using the pseudolattice factor approach

Significance

Nanometer-sized materials (i.e., nanoparticles) can be used as building blocks to construct crystalline materials structured with high resolution. The specific arrangements that nanoparticles form can be controlled by their physical shape and size, as well as the molecules attached to their surfaces (i.e., ligands). In this work, DNA ligands are used as “bonds” whose sequence “encodes” which and how far apart nanoparticles interact with each other. Here, we study how the relative size of nanoparticles and DNA modulates the orientation and structural arrangement of nanoparticles within these crystalline materials and report the specific structural changes that occur for nanoparticles with different shapes. These results provide a roadmap to understand how to build nanoparticle-based materials with DNA.

Author contributions: M.N.O., M.G., M.O.d.I.C., B.L., and C.A.M. designed research; M.N.O., M.G., H.-X.L., J.A.M., and B.L. performed research; M.N.O., M.G., J.A.M., M.O.d.I.C., B.L., and C.A.M. analyzed data; and M.N.O. and C.A.M. wrote the paper.

Reviewers: A.P.A., University of California, Berkeley; and N.A.K., University of Michigan.

The authors declare no conflict of interest.

¹M.N.O. and M.G. contributed equally to this work.

²To whom correspondence should be addressed. Email: chadnano@northwestern.edu.

This article contains supporting information online at www.pnas.org/lookup/suppl/doi:10.1073/pnas.1611808113/-DCSupplemental.

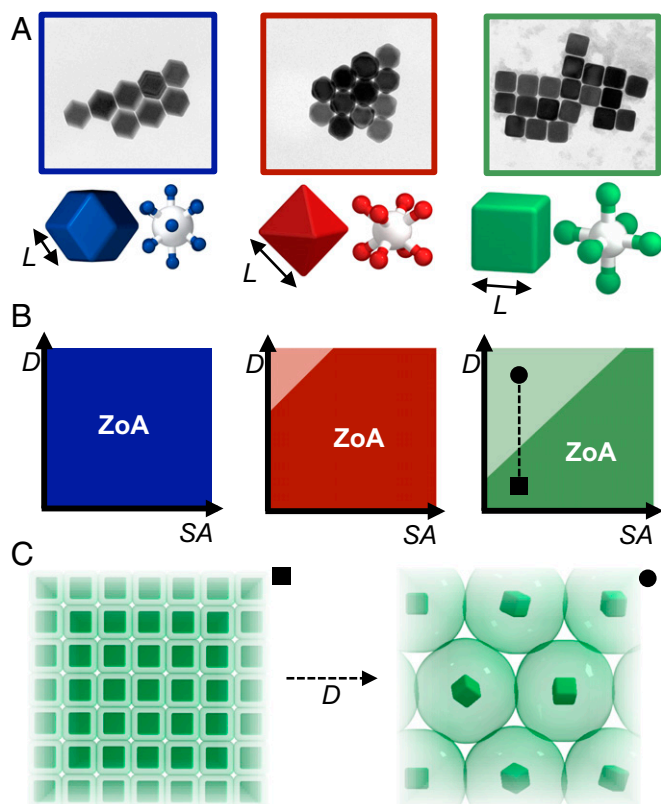


Fig. 1. Polyhedral nanoparticles with different symmetries can be functionalized with DNA and used as building blocks to study nanoscale crystallization processes. (A) EM images of cube (green), octahedron (red), and rhombic dodecahedron (blue) nanoparticles used in this work shown in order of increasing particle symmetry. Below each image is a model of the particle shape and a corresponding ball-and-stick diagram to indicate the symmetry. Nanoparticle edge length (L) is indicated next to each shape. (B) The phase space encoded by DNA length (D) and nanoparticle surface area (SA) is depicted for each symmetry nanoparticle. The darker color region in each phase diagram indicates the zone of anisotropy (ZoA). (C) The phase transition depicted by the dashed line in B, wherein L is fixed as D is increased, is shown, wherein the anisotropy of the particle core is lost.

(SI Materials and Methods) (16, 24, 25) and compared with experimental data to determine crystal symmetry, lattice parameters, and particle orientation. Importantly, use of a slow crystallization procedure and highly uniform building blocks minimizes the formation of defects and kinetically trapped states, which enables increased crystalline domain sizes, crystalline formation over a wider range of conditions, and more definitive assignments of thermodynamic phase boundaries relative to previous reports (13).

To elucidate the zone of anisotropy for each particle shape, five SA and five D were investigated, beginning with high-symmetry rhombic dodecahedra (Fig. 2A and B, Fig. S1, and Table S2). Rhombic dodecahedra can pack with 100% efficiency when the 12 rhombus-shaped facets on a given nanoparticle align face-to-face with their neighbors in a crystalline phase (i.e., both translational and orientational order) with face-centered cubic (FCC) symmetry (20, 26). Soft interactions similarly predict an FCC crystalline phase, due to the greater number of DNA hybridization events that arise from face-to-face interactions (13). As SA decreases in these experiments (for a fixed D), one might expect that fewer DNA strands per facet would lead to a smaller enthalpic driving force for the crystalline phase and thus a transition to a plastic crystal phase (i.e., translational order, but orientational disorder) with FCC symmetry, as expected for

spheres. Similarly, as D increases (for a fixed SA), one might expect that the greater free volume available to each sticky end would lead to an entropic driving force that decreases the directionality of interparticle interactions and results in a plastic crystal transition. Contrary to these expectations, FCC crystalline phases (Fig. 2A and B) were observed for all but the sample with the smallest SA and largest D , and thus the zone of anisotropy encompasses nearly the totality of the investigated phase space. A linear increase in the lattice parameter (a) with D supports the crystalline phase assignment, and the slope of ~ 0.28 nm per base pair agrees with previous work for face-to-face interactions (Table S2) (13, 16).

To further understand how nanoparticle symmetry affects the zone of anisotropy, the crystallization of octahedra was similarly investigated (Fig. 2D and E, Fig. S1, and Table S3). The dense packing of hard octahedra varies based on corner truncation or rounding (27–29), where body-centered cubic (BCC) or body-centered tetragonal (BCT) crystalline phases are favored for truncated octahedra (26, 29), and BCC or FCC plastic crystals are favored for rounded octahedra (28, 30). In experimental systems, the hydrodynamic particle shape deviates from an ideal octahedron in favor of a BCC crystalline phase (13). Similar to the rhombic dodecahedra described above, the zone of anisotropy for octahedra (i.e., a crystalline phase with BCC symmetry) fills the majority of the investigated phase space (Fig. 2E). Unlike the rhombic dodecahedra, however, a phase transition and lattice compression occurred for larger SA octahedra at shorter D —from a BCC crystalline phase to a FCC plastic crystal, as D increased (Fig. 2D).

To understand the origin of these phase transitions, nanoparticles were modeled with molecular dynamics (MD) simulations. These simulations build upon previous work that has been shown to accurately predict the DNA-mediated crystallization behavior of spherical particles (23, 31–35); however, the broken symmetry of polyhedra requires additional considerations (SI Discussion and Tables S5–S7). Although the experimentally investigated samples are too large to model exactly, SA and D were scaled to a computationally accessible size regime in a manner consistent with experiments, and DNA density was set based on experiments (Fig. S3 and Tables S8 and S9). In these simulations, a collection of particles was fixed into a lattice with a specified symmetry then allowed to relax at a temperature slightly below the crystal melting temperature to evaluate stability (i.e., whether the structure reaches equilibrium). Through comparison of different lattices for each particle symmetry and size (e.g., a BCC crystalline phase and an FCC plastic crystal), one can evaluate the thermodynamically preferred phase and extract structural parameters from the system, including lattice parameters, the fraction of DNA strands hybridized per particle (F , enthalpic contributions), and the closest average distance between two adjacent DNA strands on a single particle (entropic contributions).

As observed with experiments, the crystalline phase for rhombic dodecahedra was preferred for smaller SA and larger D compared with octahedra (Fig. 2C and F), with both shapes eventually transitioning to plastic FCC crystals. Furthermore, a linearly increased with D for all sizes of rhombic dodecahedra (Table S8) and lattice compression was observed for octahedra in plastic FCC crystals (Table S9), consistent with experiments. Calculations show that the observed transitions originate from ligand-based entropic and enthalpic contributions. In particular, an increased average inter-DNA spacing on the particle and lattice compression both indicate a wider range of less-oriented DNA states, and thus an increased free volume accessible to each DNA sticky end (32). This flexibility also allows for more DNA connections to be made between particles, as indicated by a greater F .

Based on these results, it was hypothesized that a further reduction in particle symmetry should lead to a smaller zone of anisotropy with a phase transition at larger SA and shorter D . More specifically, the increased sphericity of high-symmetry

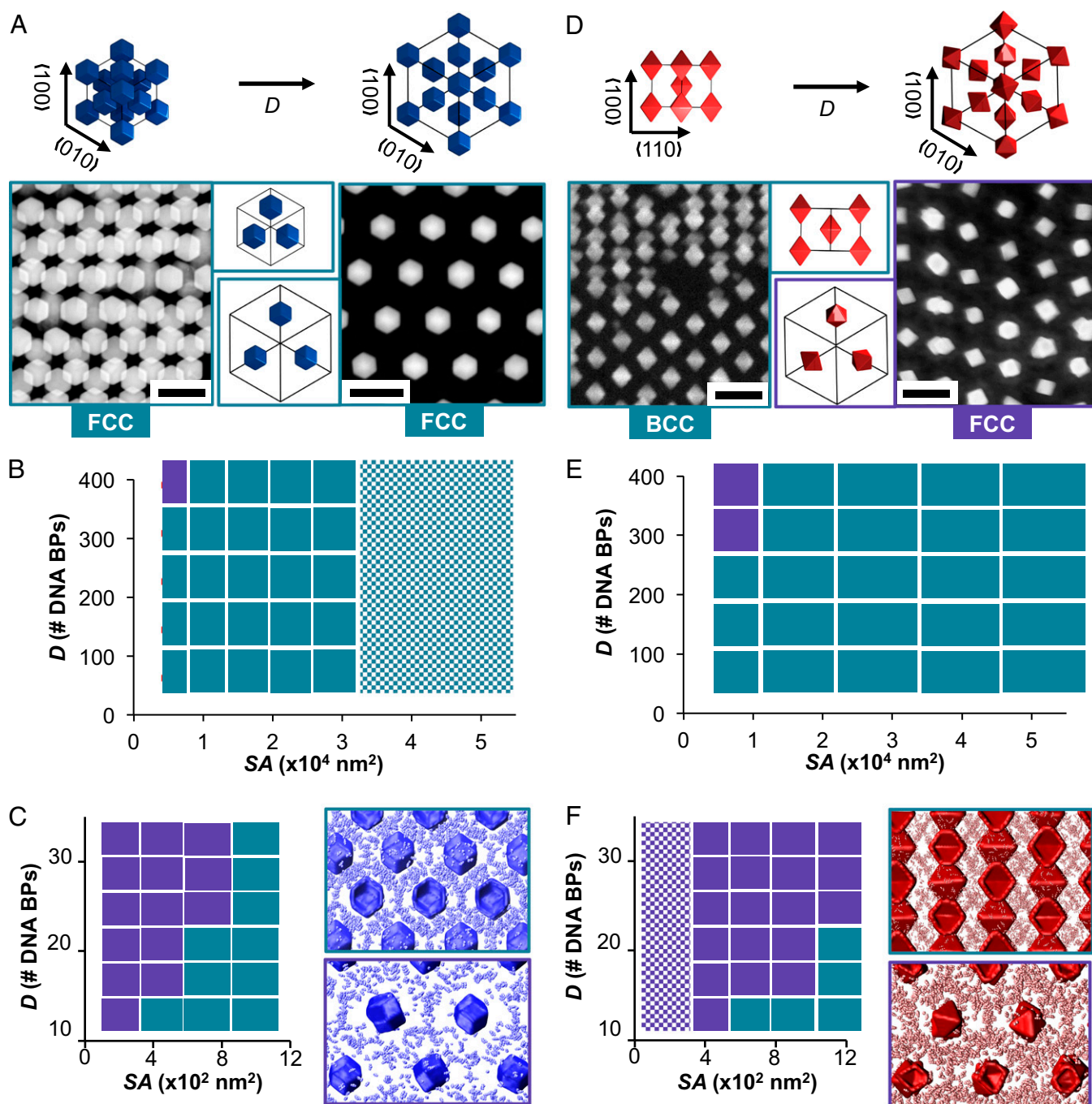


Fig. 2. The crystallization behavior of high symmetry polyhedra exhibits limited complexity as a function of D and L . (A) An FCC crystalline phase is observed for the majority of the phase space investigated for rhombic dodecahedra. To-scale unit cells are shown at top, with lattice vectors, for small and large values of D . EM images corresponding to the unit cells are provided below, with an inset from the unit cell to show particles in the same lattice plane. Throughout this figure, turquoise represents the zone of anisotropy (i.e., a crystalline phase), and purple represents a plastic crystal phase. (Scale bars, 200 nm.) (B) The experimental phase diagram for rhombic dodecahedra is shown as a function of D and SA . The checkered region indicates an extrapolation for larger, more experimentally challenging sizes of rhombic dodecahedra as experiments, for systems that have been scaled to smaller, computationally more accessible sizes in a manner consistent with experiments. (C) MD simulations confirm the same phase transition observed for rhombic dodecahedra as experiments, for systems that have been scaled to smaller, computationally more accessible sizes in a manner consistent with experiments. The spatial distribution of DNA sticky ends is shown at right for each phase, where the DNA is localized between particles for the crystalline phase and more isotropically distributed for the plastic phase. (D) As D increases for the smallest L of octahedra investigated, a phase transition from a BCC crystalline phase to an FCC plastic crystal is observed. (E) Experimental phase diagram over the same range of D and L shows that the zone of anisotropy occupies a smaller area of the phase space relative to the rhombic dodecahedra. (F) MD simulations (for particles with similar SA as the rhombic dodecahedra) confirm the observed phase behavior.

particles should result in a more diffuse DNA distribution (i.e., reduced number of DNA strands per facet) and a greater free volume available to each DNA strand. Thus, as D increases, the resultant increase in charge repulsion and free volume

should not contribute as significantly as they do for lower-symmetry particles.

To test this hypothesis, the crystallization of cubes with comparable SA and D was investigated (Fig. 3, Figs. S1 and S2,

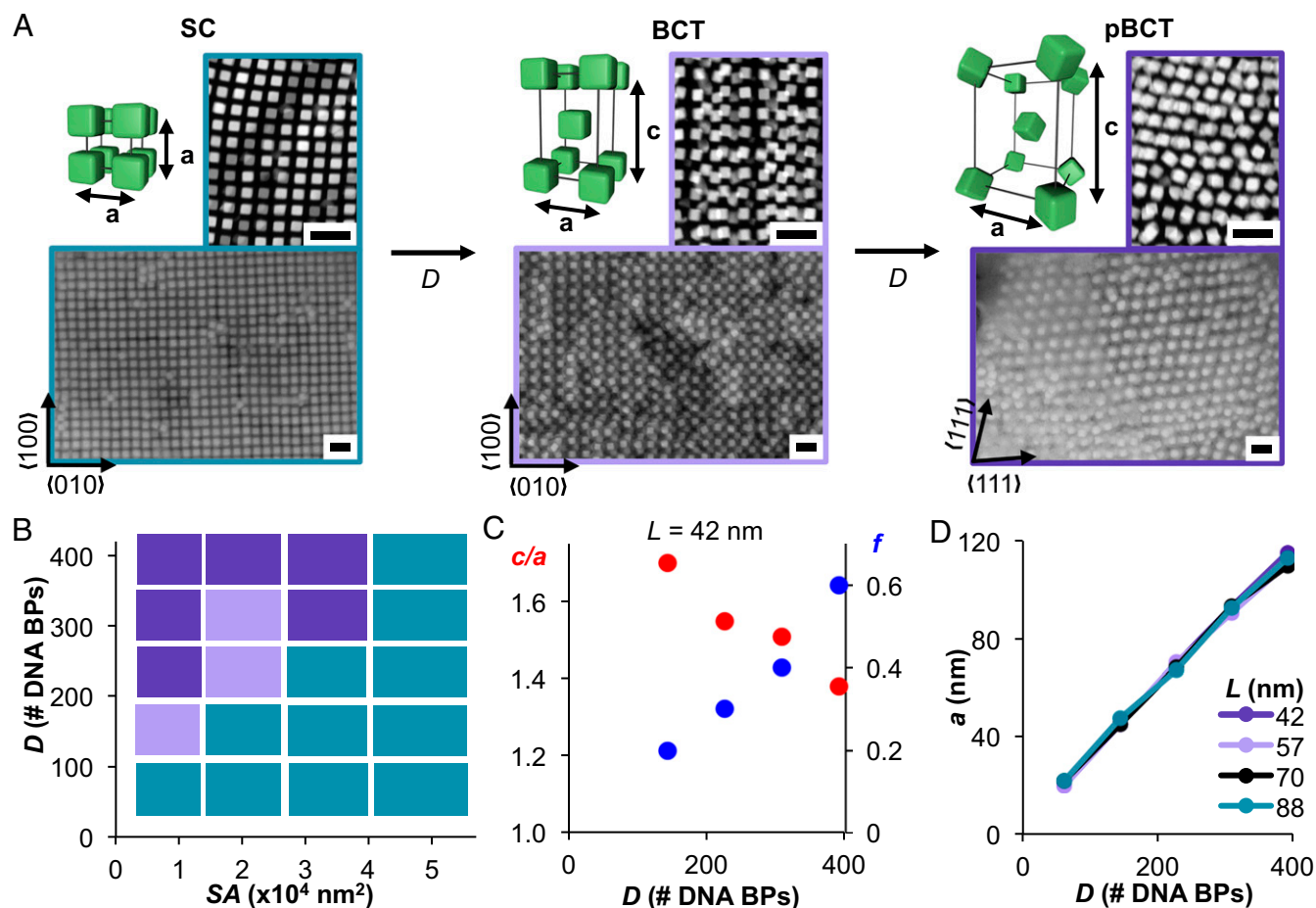


Fig. 3. Experimental investigation into cube crystallization behavior shows two continuous phase transitions as a function of D and L . (A) As D increases for a given L (shown here as $L = 57 \text{ nm}$), cubes crystallize with (from left to right) SC (crystalline), BCT (crystalline), and FCC (plastic) symmetries. For each symmetry, a unit cell is given, with the lattice parameters a and c indicated. Next to each unit cell is a TEM image of silica-embedded lattices sectioned along a particular crystallographic plane. Below each unit cell is an SEM image of silica-embedded lattices, with the lattice vectors indicated at bottom left. (Scale bars, 200 nm.) (B) Phase diagram for cubes as a function of D and SA , colored based on the symmetry—SC (turquoise) or BCT (purple)—where each box is centered on a single experimental data point. (C) For the smallest cube size investigated ($L = 42 \text{ nm}$), the data for BCT phases are shown as a function of D . As D increases, c/a decreases and f increases. (D) The lattice parameter, a , increases linearly with D for all L investigated.

and Table S4). Cubes densely pack into a simple cubic (SC) crystalline phase, with slight distortions in orientation for mildly truncated or rounded corners, or a plastic or crystalline FCC phase for high degrees of imperfection (20, 27–30, 36–38). Indeed, a smaller zone of anisotropy was observed for cubes relative to octahedra and rhombic dodecahedra, consistent with the above hypothesis. Outside of this zone, two phase transitions were observed as SA decreases and D increases that involve a change of Bravais lattice: a first-order transition from an SC crystalline phase to a BCT crystalline phase, followed by a continuous transition to a BCT plastic crystal (Fig. 3). The presence of an intermediate crystalline phase with an interaction symmetry distinct from the nanoparticle shape represents an unexpected observation. Interestingly, despite the change from cubic to tetragonal for the first transition, a (i.e., the minor dimension in the square plane for the BCT phase and the only dimension for the cubic phases) increases linearly with D for all investigated SA , with the same rise per base pair as observed for rhombic dodecahedra and octahedra (Fig. 3). This result suggests that nanoparticles consistently hybridize to one another along two axes, the (100) and (010) as defined by the symmetry of the final lattice, whereas symmetry breaks along the third axis, the (001). The continuous nature of the latter transition can be seen from an orientational order factor (f , ranges from 0 for perfectly oriented to

1 for randomly oriented) determined from comparison between experimental and modeled SAXS data (Fig. 3C and Table S4). This change in f occurs as the c/a ratio for the tetragonal unit cell decreases from ~ 1.7 to ~ 1.4 (consistent with an FCC symmetry) (Fig. 3C). These results are consistent with our hypothesis that lower-symmetry particles would possess a smaller crystalline region of the phase space, but with more complexity than expected.

To understand the origins of these phase transitions, cubes were simulated with MD (Fig. 4, Figs. S4–S8, and Table S10). Importantly, phase transitions and lattice parameters consistent with experiments were observed as a function of SA and D (Fig. 4). Close inspection of the spatial distribution and angles of DNA engaged in hybridization shows that the symmetry breaking from SC to BCT phases originates from an unexpected symmetry breaking in the ligand distribution (Figs. S5 and S6). More specifically, the distances between DNA sticky ends are greater on the BCT (001), relative to the BCT (100) and (010), whereas all faces possess equivalent DNA distances in the SC and plastic BCT phases. Similar behavior is observed in the orientation angle of DNA molecules with respect to the nanoparticle surface, wherein larger angles on the BCT (001) indicate reduced face-to-face interactions. Interestingly, the broken symmetry of the DNA distribution becomes more pronounced away from the particle surface, where the DNA can explore a greater free

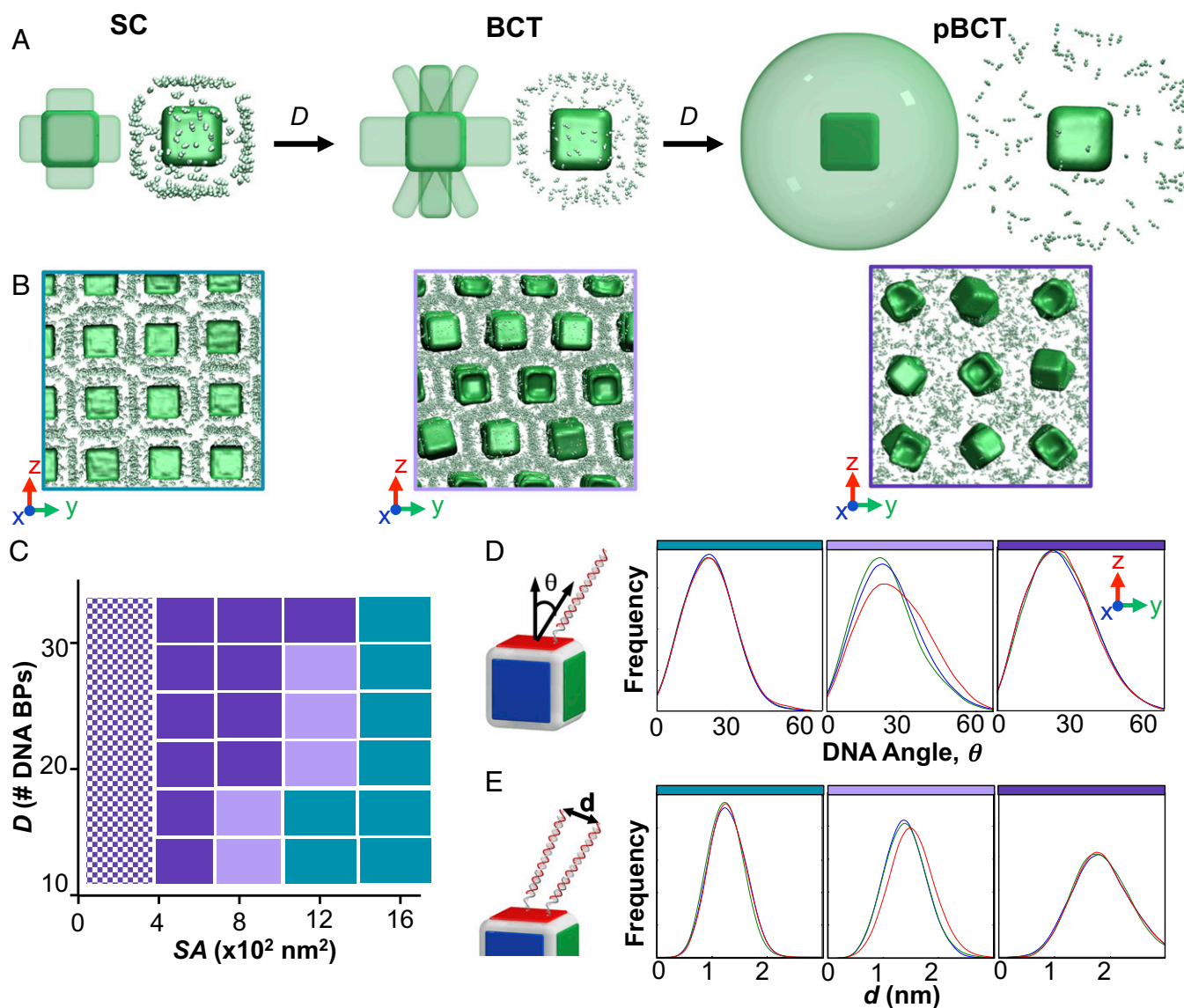


Fig. 4. MD simulations of cube crystallization reveal that phase transitions occur due to a novel symmetry breaking of the ligand distribution. (A) As D increases in these systems, the distribution of DNA ligands breaks symmetry along the (001). Specifically, the DNA originally on the (001) splits apart and begins to point toward the edges of the (001), such that it can attach to four cubes. As D is increased further, these four interactions become increasingly spaced apart due to electrostatic and free volume arguments. A model (Left) and image from an MD simulation (Right) are shown to indicate the distribution of DNA sticky ends. (B) MD simulations along particular crystallographic planes reveal the distribution of DNA sticky ends between particles. Planes shown are (100) for SC, (100) for BCT, and (110) for the plastic BCT. (C) A phase diagram based on simulation results confirms the same trends in phase and particle orientation as observed in experiment. The colors are consistent with Fig. 3 and the checkered region indicates an extrapolation. (D) DNA angle (θ) with respect to an ideal angle of 0 (perpendicular to the surface) shows a broken symmetry for the DNA on the (001) of the BCT crystalline phase only (red). (E) Distance between DNA sticky ends (d) similarly shows that symmetry breaking for the BCT phase occurs away from the particle surface (red). Comparison between the three symmetries further shows that as DNA length increases, the distribution of DNA distances also increases due to the greater free volume accessible.

volume. This occurs, in part, because the dense DNA shell near the surface of the particle restricts the position of the DNA. Simulations with and without a dense DNA shell near the surface indeed show that this dense shell is necessary to observe the transition to a BCT symmetry (Fig. S8).

Collectively, these deviations allow each cube in the crystalline BCT lattice to hybridize to four neighbors in a face-to-face fashion along the BCT (100) and (010), similar to SC lattices, but to four neighbors above and four below along the BCT (001). Simulations indicate that the observed transitions predominantly originate from the enthalpy and entropy of the DNA, rather than the packing entropy of the particle shape (Fig. 4) (20, 30). In particular, we hypothesize that the DNA shell breaks symmetry

as D increases to (i) reduce the electrostatic repulsion associated with a longer DNA backbone, (ii) increase the free volume available to the DNA, especially at the sticky ends (as discussed above), and (iii) ultimately increase the number of DNA hybridization events that connect nanoparticles within the lattice. The lack of a corollary symmetry in the nanoparticle, or preferred orientation of the (001) with respect to the experimental environment or crystallization conditions, suggests that symmetry breaks upon addition to the lattice, driven by the local DNA environment. These hypotheses are consistent with the transition from crystalline BCT to plastic BCT, and the decrease in the plastic BCT c/a ratio, as D further increases—both of which coincide with an increase in the distance between DNA strands and DNA angle. This unique behavior

highlights the importance of considering both particle and ligand effects in nanoparticle crystallization.

This work defines the phase space where directional interactions persist for programmable atom equivalents consisting of anisotropic nanoparticle cores as “atoms” and DNA ligands as “bonds.” The understanding gained from this work establishes the range of conditions where design rules based on geometric considerations can be used to predict crystal structure. If these results were extended to lower-symmetry particles (e.g., tetrahedra), one would imagine an even smaller zone of anisotropy and richer phase diagram, including the possibility of quasicrystal or diamond lattices (20, 30, 36, 39). Due to the highly modular and programmable nature of nucleic acids, the location of these phase transitions can likely be tuned depending on the desired structure, via modulation of the design (e.g., flexibility) (40) or the type of nucleic acid used (e.g., locked nucleic acid or RNA) (41). Beyond defining the zone of anisotropy, this work also establishes a strategy to assemble nonspherical building blocks into a rich set of different phases based on the interplay of the particle and ligand structure.

ACKNOWLEDGMENTS. This work was supported by Air Force Office of Scientific Research Multidisciplinary University Research Initiative FA9550-11-1-0275, National Science Foundation (NSF) Materials Research Science and Engineering Center (MRSEC) program Grant DMR-1121262 at the Materials Research Center of Northwestern University (NU), and the Non-equilibrium Energy Research Center, an Energy Frontier Research Center funded by the Department of Energy (DoE), Office of Science, and Office of Basic Energy Sciences under Award DE-SC0000989 (all to C.A.M. and M.O.d.I.C.). M.N.O. was supported by a National Science Foundation Graduate Research Fellowship and M.G. by Natural Sciences and Engineering Research Council of Canada graduate fellowship Grant PGS-D 6799-459278-2014. H.-X.L. was supported by a scholarship from China Scholarship Council under Grant 201306310060. J.A.M. was supported by the International Institute of Nanotechnology through a postdoctoral fellowship. SAXS experiments were carried out at the Dupont–Northwestern–Dow Collaborative Access Team beamline at the Advanced Photon Source (APS) at Argonne National Laboratory, and use of the APS was supported by DoE Grant DE-AC02-06CH11357. This work made use of the EPIC facility (NUANCE Center at Northwestern University), which has received support from the MRSEC program (NSF Grant DMR-1121262) at the Materials Research Center, the International Institute for Nanotechnology (IIN), and the State of Illinois, through the IIN. Microtoming was performed at the NU Biological Imaging Facility generously supported by the NU Office for Research.

1. Mirkin CA, Letsinger RL, Mucic RC, Storhoff JJ (1996) A DNA-based method for rationally assembling nanoparticles into macroscopic materials. *Nature* 382(6592): 607–609.
2. Alivisatos AP, et al. (1996) Organization of ‘nanocrystal molecules’ using DNA. *Nature* 382(6592):609–611.
3. Shevchenko EV, Talapin DV, Kotov NA, O’Brien S, Murray CB (2006) Structural diversity in binary nanoparticle superlattices. *Nature* 439(7072):55–59.
4. Min Y, Akbulut M, Kristiansen K, Golan Y, Israelachvili J (2008) The role of interparticle and external forces in nanoparticle assembly. *Nat Mater* 7(7):527–538.
5. Bishop KJM, Wilmer CE, Soh S, Grzybowski BA (2009) Nanoscale forces and their uses in self-assembly. *Small* 5(14):1600–1630.
6. Jones MR, Osberg KD, Macfarlane RJ, Langille MR, Mirkin CA (2011) Templated techniques for the synthesis and assembly of plasmonic nanostructures. *Chem Rev* 111(6):3736–3827.
7. Jones MR, Seeman NC, Mirkin CA (2015) Nanomaterials. Programmable materials and the nature of the DNA bond. *Science* 347(6224):1260901.
8. Batista CA, Larson RG, Kotov NA (2015) Nonadditivity of nanoparticle interactions. *Science* 350(6257):1242477.
9. Choi CL, Alivisatos AP (2010) From artificial atoms to nanocrystal molecules: Preparation and properties of more complex nanostructures. *Annu Rev Phys Chem* 61: 369–389.
10. Macfarlane RJ, O’Brien MN, Petrosko SH, Mirkin CA (2013) Nucleic acid-modified nanostructures as programmable atom equivalents: Forging a new “table of elements”. *Angew Chem Int Ed Engl* 52(22):5688–5698.
11. Park SY, et al. (2008) DNA-programmable nanoparticle crystallization. *Nature* 451(7178):553–556.
12. Nykypanchuk D, Maye MM, van der Lelie D, Gang O (2008) DNA-guided crystallization of colloidal nanoparticles. *Nature* 451(7178):549–552.
13. Jones MR, et al. (2010) DNA-nanoparticle superlattices formed from anisotropic building blocks. *Nat Mater* 9(11):913–917.
14. Macfarlane RJ, et al. (2011) Nanoparticle superlattice engineering with DNA. *Science* 334(6053):204–208.
15. Di Michele L, Eiser E (2013) Developments in understanding and controlling self assembly of DNA-functionalized colloids. *Phys Chem Chem Phys* 15(9):3115–3129.
16. O’Brien MN, Jones MR, Lee B, Mirkin CA (2015) Anisotropic nanoparticle complementarity in DNA-mediated co-crystallization. *Nat Mater* 14(8):833–839.
17. Rogers WB, Manoharan VN (2015) DNA nanotechnology. Programming colloidal phase transitions with DNA strand displacement. *Science* 347(6222):639–642.
18. Kim Y, Macfarlane RJ, Jones MR, Mirkin CA (2016) Transmutable nanoparticles with reconfigurable surface ligands. *Science* 351(6273):579–582.
19. Liu W, et al. (2016) Diamond family of nanoparticle superlattices. *Science* 351(6273): 582–586.
20. Damasceno PF, Engel M, Glotzer SC (2012) Predictive self-assembly of polyhedra into complex structures. *Science* 337(6093):453–457.
21. O’Brien MN, Jones MR, Brown KA, Mirkin CA (2014) Universal noble metal nanoparticle seeds realized through iterative reductive growth and oxidative dissolution reactions. *J Am Chem Soc* 136(21):7603–7606.
22. Laramy CR, Brown KA, O’Brien MN, Mirkin CA (2015) High-throughput, algorithmic determination of nanoparticle structure from electron microscopy images. *ACS Nano* 9(12):12488–12495.
23. Auyeung E, et al. (2014) DNA-mediated nanoparticle crystallization into Wulff polyhedra. *Nature* 505(7481):73–77.
24. Senesi AJ, Lee B (2015) Small-angle scattering of particle assemblies. *J Appl Cryst* 48(4):1172–1182.
25. Li T, Senesi AJ, Lee B (April 7, 2016) Small angle X-ray scattering for nanoparticle research. *Chem Rev*, 10.1021/acs.chemrev.5b00690.
26. Agarwal U, Escobedo FA (2011) Mesophase behaviour of polyhedral particles. *Nat Mater* 10(3):230–235.
27. Henzie J, Grünwald M, Widmer-Cooper A, Geissler PL, Yang P (2011) Self-assembly of uniform polyhedral silver nanocrystals into densest packings and exotic superlattices. *Nat Mater* 11(2):131–137.
28. Ni R, Gantapara AP, de Graaf J, van Roij R, Dijkstra M (2012) Phase diagram of colloidal hard superballs: From cubes via spheres to octahedra. *Soft Matter* 8(34):8826–8834.
29. Gantapara AP, de Graaf J, van Roij R, Dijkstra M (2013) Phase diagram and structural diversity of a family of truncated cubes: Degenerate close-packed structures and vacancy-rich states. *Phys Rev Lett* 111(1):015501.
30. van Anders G, Ahmed NK, Smith R, Engel M, Glotzer SC (2014) Entropically patchy particles: Engineering valence through shape entropy. *ACS Nano* 8(1):931–940.
31. Li Ti, Sknepnek R, Macfarlane RJ, Mirkin CA, de la Cruz MO (2012) Modeling the crystallization of spherical nucleic acid nanoparticle conjugates with molecular dynamics simulations. *Nano Lett* 12(5):2509–2514.
32. Thaner RV, et al. (2015) Entropy-driven crystallization behavior in DNA-mediated nanoparticle assembly. *Nano Lett* 15(8):5545–5551.
33. Knorowski C, Burleigh S, Travesset A (2011) Dynamics and statics of DNA-programmable nanoparticle self-assembly and crystallization. *Phys Rev Lett* 106(21): 215501.
34. Anderson JA, Lorenz CD, Travesset A (2008) General purpose molecular dynamics simulations fully implemented on graphics processing units. *J Comput Phys* 227(10): 5342–5359.
35. Glaser J, et al. (2015) Strong scaling of general-purpose molecular dynamics simulations on GPUs. *Comput Phys Commun* 192:97–107.
36. Torquato S, Jiao Y (2009) Dense packings of the Platonic and Archimedean solids. *Nature* 460(7257):876–879.
37. Zhang Y, Lu F, van der Lelie D, Gang O (2011) Continuous phase transformation in nanocube assemblies. *Phys Rev Lett* 107(13):135701.
38. Batten RD, Stillinger FH, Torquato S (2010) Phase behavior of colloidal superballs: Shape interpolation from spheres to cubes. *Phys Rev E Stat Nonlin Soft Matter Phys* 81(6 Pt 1):061105.
39. Boles MA, Talapin DV (2014) Self-assembly of tetrahedral CdSe nanocrystals: Effective “patchiness” via anisotropic steric interaction. *J Am Chem Soc* 136(16):5868–5871.
40. Senesi AJ, et al. (2014) Oligonucleotide flexibility dictates crystal quality in DNA-programmable nanoparticle superlattices. *Adv Mater* 26(42):7235–7240.
41. Barnaby SN, et al. (2015) Modular and chemically responsive oligonucleotide “bonds” in nanoparticle superlattices. *J Am Chem Soc* 137(42):13566–13571.